Fano resonance of optical phonons in a multilayer graphene stack

Masahiro Kitajima[1,2]*, Ikufumi Katayama[2]*, Ørjan Sele Handegård[1,3], Tadaaki Nagao[1,3]*, Shohei Chiashi[4], Shigeo Maruyama[4], and Jun Takeda[2]

[1]International Center for Materials Nanoarchitectonics, National Institute for Materials Science (NIMS), 1-1 Namiki, Tsukuba, Ibaraki 305-0044, Japan

[2]Department of Physics, Faculty of Engineering Science, Yokohama National University, Yokohama 240-8501, Japan

[3]Department of Condensed Matter Physics Graduate School of Science Hokkaido University Kita-10 Nishi-8 Kita-ku, Sapporo 060-0810, Japan

[4]Department of Mechanical Engineering, The University of Tokyo, 7-3-1 Hongo, Bunkyo-ku, Tokyo, 113-8656, Japan

*corresponding authors: kitajima.masahiro@nims.go.jp; kitajima-masahiro-kj@ ynu.ac.jp; katayama-ikufumi-bm@ynu.ac.jp; nagao.tadaaki@nims.go.jp

Abstract

We studied Fano interference between the Raman spectrum of G-band phonons and electron continuum in a multilayer graphene stack. The thickness and power dependencies of the Fano interference coefficient $|1/q|$ in the G-mode, where q is the Fano asymmetry parameter, were spatially visualized and analyzed using the Gaussian–convoluted Breit–Wigner–Fano function. The estimated $|1/q|$ decreases with an increase in the layer number

and laser power in the low-power region at least up to for monolayer, bilayer, and trilayer graphene. In the higher-power region, $|1/q|$ increases with power only for monolayer graphene. The observed behaviors of $|1/q|$ reflect the phase difference of Raman signals from the electron continuum and G-band and possibly originate from changes in the electronic relaxation time and the Fermi level of graphene owing to the laser heating of the sample.

Introduction

Graphene, a monolayer carbon sheet, has attracted considerable interest since its discovery, owing to its many intriguing physical, optical, mechanical, and electric properties that are useful for future electric devices and applications [1-4]. Raman spectroscopy has been extensively used to characterize both electronic and phonon properties of graphene and related materials [5-12]; it provides useful information about structural and electronic properties. Raman imaging is a powerful method for obtaining spatially resolved vibrational spectra and information about the interactions with electronic band structures in graphene. For example, Raman imaging allows us to determine graphene structures, including the number of graphene sheets [6,10,11,13], defect [14] or doping [15] distributions, and interlayer interactions [12], in a quick and nondestructive manner.

One of important physical properties that can be investigated by Raman spectroscopy is electron–phonon interactions. Electron–phonon interactions near the Dirac point result in phenomena such as the Kohn anomaly. This effect is discussed based on changes in the band width (damping rate) and frequency shifts of G- (the Γ-point C–C stretching mode) and 2D

(second-order harmonics of the disorder-induced band D) bands in the Raman spectrum of graphene, which are induced by electron or hole doping by applying gate DC biases [9,16]. Quantum interference between a discrete phonon state and an electron continuum will result in peak asymmetry of the phonon state, known as the Fano interference [17], which provides important information about electron–phonon coupling. In this study, we demonstrate that Raman imaging provides us with a new insight into the latter effect, i.e., the Fano interference.

Originally, the Fano interference has been proposed for a discrete auto-ionized state and a continuum in He atoms. Then, this model has been applied to the interference between Raman signals from electrons and optical phonons in doped Si [18], and many interesting results have been obtained in various materials to date. The line shape of a phonon spectrum with the Fano interference is provided based on the Breit–Wigner–Fano (BWF) line shape [19] using

$$I_{\mathrm{BWF}}(\omega;\ \omega_G) = I_0 \frac{(1+2(\omega-\omega_G)/q\gamma)^2}{1+4(\omega-\omega_G)^2/\gamma^2}, 1)$$

where I_0, ω_G, γ, and q are the peak intensity, spectral peak frequency, spectral width, and the Fano asymmetry parameter, respectively. The interference between Raman signals from discrete and continuum states results in an asymmetric spectral line shape, and the asymmetry is proportional to a dimensionless parameter $1/q$, the Fano interference coefficient [20,21]. When $1/q = 0$, equation 1) is a Lorentz function. The Fano asymmetry parameter q is given by

$$q = \frac{V(A_G/A_e)+V^2 R(\varepsilon)}{\pi V^2 \rho(\varepsilon)}, 2)$$

where A_G and A_e are the transition amplitudes for the phonon discrete and electron continuum states, respectively; V is the coupling constant between the discrete and continuum states;

$\rho(\varepsilon)$ is the density of the continuum state; and $\pi^{-1}R(\varepsilon)$ is the Hilbert transform of the electronic Raman response [19]. This equation indicates that q depends on the amplitude ratio of Raman signals from discrete phonon states to those from an electronic continuum and on the phase difference between electron–electron coupling and electron–phonon coupling.

For carbon-related materials, the Fano asymmetry parameter for G-band phonons was observed in graphite intercalation compounds [22], metallic single-walled carbon nanotubes (CNT) [23] and CNT bundles [24]. For few-layer graphene flakes, Ferrari and his group reported that the interlayer shear mode (C_2) exhibits a clear Fano asymmetric shape because the low-energy phonon (approximately 31 cm^{-1}) makes it easier to couple with near-Dirac point low-energy quasiparticles that have large oscillator strength [20]. Although this effect becomes small for the G-mode with high frequency, Yoon et al. measured Raman scattering with varying back-gate bias for graphene layers and determined that the Raman G-band of single-layer graphene exhibits an asymmetric line shape near the charge-neutrality point [21,25]. For bilayer epitaxial graphene, the Fano line shapes of the G-mode close to 1,590 cm^{-1} have been reported using infrared reflectivity spectroscopy [26,27]. However, until now, there have been no systematic investigations on the layer number dependence of Fano interference in graphene. In this study, we demonstrate that Raman imaging is a powerful technique for unveiling the Fano interference of graphene depending on the layer number and excitation power, even though the observed asymmetry is small.

Thus far, there have been many published papers on Raman imaging of graphene, whose samples are, in most cases, isolated flakes exfoliated from graphite with different layer

numbers and uneven crystalline orientation. Most of the studies are on the mapping of spectral intensity, frequency, and bandwidth for phonon bands (G, D, and 2D bands), whereas the Fano asymmetry parameter remains to be investigated in detail in a systematic manner. In this study, we fabricated well-stacked multilayer graphene with a hexagonal shape, whose crystalline orientation is well defined [28,29], and performed systematic Raman imaging of multilayer graphene stacks with a specific focus on imaging the Fano asymmetry in G-mode optical phonons to understand the phase difference of electron–electron coupling and electron–phonon coupling.

Experiment

Spatially resolved confocal Raman spectroscopy was performed at room temperature using the Witec-Alpha300SRA system with a frequency-doubled Nd:YAG laser as an excitation source. The excitation wavelength for Raman scattering was 532 nm, and the power was tunable between 0.2 and 25 mW. We measured Raman spectra through an objective lens with a numerical aperture of 0.80, and the spot size of the excitation laser was approximately 400 nm at the diffraction limit.

The graphene stack sample was grown by chemical vapor deposition from a mixture of ethanol and hydrogen gas on a Cu substrate heated at ~1,000°C. Then, the obtained graphene stack was transferred onto a SiO_2 (300 nm)/Si substrate. The formed multilayer graphene exhibited hexagonal shapes, which indicated good crystallinity throughout the entire sample, as observed in the microscopic picture in the inset in Fig. 1(a) (for details, see elsewhere [28,29]). Such similitude of layers observed in the microscopic image indicates that crystal

orientations are well defined, which is established by a well-controlled layer-by-layer growth of graphene in our setup [30]. Of note, although AB stacking is originally confirmed by electron diffraction [28,29], tiny adsorptions or other external stimuli may slightly change stacking as in reference [31].

Results and discussion

1. Raman mapping

Figure 1(a) shows a typical Raman spectrum of the multilayer graphene stack obtained with 532 nm excitation at 0.23 mW; characteristic Raman bands for the optical phonons in graphene are observed. The peaks at approximately 1,580 and 2,690 cm^{-1} are attributed to G and 2D ($2 \times D$) bands, respectively. The peaks at approximately 3,250 and 4,280 cm^{-1} correspond to 2G ($2 \times G$) and 2DG ($2 \times D + 1 \times G$), respectively. The peak at 520 cm^{-1} is the signal from the Si substrate.

Before discussing Fano interference imaging, we show intensity mapping for typical phonon modes in Figs. 1(b)–1(d). The intensity map of the G-band indicates a hexagonal shape [Fig. 1(b)], which indicates the layer number in the multilayered graphene stack [see also the optical image in the inset in Fig. 1(a)]. Correspondingly, the intensity of the Raman signal from the Si substrate monotonically decreases, which indicates the layer number dependence of graphene absorption in our sample. By contrast, the 2D band intensity only slightly depends on the layer number owing to the difference in the Raman process; the G-band originates from the first-order Raman process, and the 2D band originates from the doubly resonant second-order Raman-scattering process [32]. We can confirm the

monotonous increase of the G-band intensity using the layer number, as illustrated in Fig. 1(e).

Figure 2 illustrates the obtained maps of parameters estimated by fitting the spectrum using the BWF function 1) at the 1- and 2-ML border with the laser power of 0.23 mW. The intensity mapping of the G-band is illustrated in Fig. 2(a). We can also clearly observe the difference in the frequency [Fig. 2(b)], spectral width [Fig. 2(c)], and, surprisingly, $|1/q|$ [Fig. 2(d)] between 1 and 2 ML. The value of $|1/q|$ is clearly stronger at 1 ML than that at 2 ML.

2. Layer number dependence

To clarify the layer number dependence of $1/q$, we averaged the area with the same layer number in Raman imaging and carefully compared the Raman spectra of the G-band with the fitting obtained using the BWF function [Eq. 1)]. The dashed lines in Fig. 3(a) are the fitting result with the BWF lineshape, indicating a small but distinct difference between the experimental data and fitting, especially at the tails of the G-band spectrum. Because the difference in $1/q$ depending on the layer number is very small, we had to first clarify the origin of this discrepancy. To minimize the discrepancy, we used the convolution of Eq. 1) with the Gaussian function as

$$I(\omega) = \int_0^\infty d\Omega \, I_{\text{BWF}}(\omega; \, \Omega) \exp\left[-\frac{(\Omega - \omega_G)^2}{2\sigma^2}\right]. \, 3)$$

A similar convolution with the Lorentzian function is known as the Voigt function, which is often used to analyze Raman spectra [33]. Here σ represents the inhomogeneous broadening of the G-band Raman peak. The solid lines in Fig. 3(a) show the fitting obtained using the BWF–Gauss function [Eq. (3)], which indicates clear improvement of the fitting

accuracy. In this fitting, the obtained parameter of $1/q$ is almost identical to the value obtained using Eq. (1), possibly because $1/q$ is the only parameter that determines the asymmetry of the spectral shape. To confirm the precision of obtained $1/q$, in Fig. 3(b), we plotted several different spectra obtained with different $1/q$ values, where a small but clear difference in spectral shapes was observed. In this case, $1/q = -0.040$ is a parameter that best fits the experimental data. Based on these results, we concluded that the obtained $1/q$ is physically meaningful; thus, it is worth discussing its origins. Hereinafter, we use $1/q$ obtained using Eq. (3), the BWF–Gauss function.

Figure 3(c) indicates the layer number dependence of $1/q$ plotted together with the center frequency of the G-band. The error bars are estimated from the fitting accuracy. When the layer number increases from 1 to 2 ML, $|1/q|$ decreases by approximately 20% of that for 1 ML. The decrease is more gradual with a further increase in layer thickness and similar to that for highly oriented pyrolytic graphite (HOPG) above 10 ML. This occurs possibly because of the enhanced phase relaxation time of the electron continuum that affects $\pi^{-1}R(\varepsilon)$, which leads to the enhanced difference in phase between the phonon Raman spectrum and the electronic continuum. The enhancement of the phase relaxation time is due to increased electron scattering to the split electronic bands [5,8,34] when the layer number increases, as will be discussed later. Of note, the dependence of the G-mode frequency illustrated in Fig. 3(c) is in good agreement with the empirical relation between the G-mode frequency and the layer number provided by Wang et al. [11]. The $1/q$ values obtained here are also consistent with those in previous studies [25,26]. The high crystallinity of our sample combined with Raman imaging simplified the observation of the small dependence of $|1/q|$ values on the

layer number. Note that parameters γ and σ only have small dependence on the layer number in our experimental condition.

3. Observation of power dependence of 1/q

To understand the electron–phonon coupling in graphene layers, we examined the laser-power dependence, which could indicate the influence of local heating of the sample, as illustrated in Fig. 4. When the sample is irradiated with a laser, its surface is heated through optical absorption. Therefore, by examining the laser-power dependence, it is possible for one to understand phases of electron–electron and electron–phonon interactions in solids at high temperature [35,36]. We implemented Raman mapping measurements as a function of laser power up to approximately 25 mW and observed a clear power dependence of $|1/q|$, as illustrated in Fig. 4(a). This power dependence is clearly visible in the Raman mapping illustrated in Figs. 4(b) and 4(c). At an approximately 25-mW power, as illustrated in Fig. 4(b), the $|1/q|$ distribution for the graphene sample indicates clear contrast between the hexagonal layers. By contrast, the $|1/q|$ distribution at low power, illustrated in Fig. 4(c), indicates a slight difference between 1 and 2 ML.

The observed value of $|1/q|$ for 1 ML is the smallest at 10 mW; then, it recovers at approximately 20 mW, as indicated by the solid circle in Fig. 4(a), which leads to the nonmonotonous power dependence. The value of $|1/q|$ decreases with an increase in power up to approximately 10 mW; then, it increases with a further increase in power. The laser-power dependence of $|1/q|$ for 2 and 3 ML graphene layers indicates that $|1/q|$ monotonically decreases with an increase in power. A similar monotonous power dependence was observed

for layers thicker than 3 ML. Note that parameters γ and σ only have small dependence on the laser power, and we only focus on the dependencies of the parameter $|1/q|$.

4. Change in the asymmetry parameter induced by light-mediated heating

High-power laser irradiation leads to changes in Raman spectra owing to sample heating [5,7,30]. We will consider this effect on the observed Fano parameter. To discuss this, we need to estimate the local temperature increase ΔT by laser irradiation. Because graphene absorption is small, we assume that graphene films are heated through the neighboring media (Si and air) under steady illumination [37]. The temperature rise can be estimated by $\Delta T = P/\left(\frac{\pi K_{\mathrm{av}} l}{2}\right)$, where P is the laser power, l is the laser spot size, and $K_{\mathrm{av}} = \frac{K_{\mathrm{Si}} + K_{\mathrm{air}}}{2}$ is the average thermal conductivity of the neighboring media. K_{Si} and K_{air} are the thermal conductivities of Si and air, respectively. We neglected the contribution from SiO$_2$ because the optical absorption is negligible for the wavelength used in this experiment. The formula for the temperature increase is similar to the solution obtained by solving the heat conduction equation for laser heating under steady state condition [38]. For example, the estimated temperature increase in our experiment was $\Delta T = 400$ K for 20 mW excitation.

- Lower-power region

We first discuss the low-power region where the $1/q$ value for every layer number decrease with an increase in laser power. Using Pfeifer's formalism [39], the Fano interference parameter q is determined using

$$q = -\cot\left(\frac{\phi}{2}\right), \quad 4)$$

where ϕ is the relative phase of the discrete state with respect to the response of the continuum

states. According to the coherent phonon experiment in silicon reported by Kato et al. [40], the phase of the continuum state is related to the relaxation time of the electronic excited state. Therefore, we considered that the temperature dependence of q would reflect the temperature dependence of the relaxation time of electronic excited states in graphene, which will be shorter at higher temperatures [41]. By extrapolating the temperature dependence of q in silicon to high temperatures [40] and normalizing the value of $1/q$ for graphene at room temperature, we obtained the dotted blue curve in Fig. 5(a) for the temperature dependence of $1/q$. The relation between $1/q$ and ϕ is determined using Eq. 2) and is plotted in Fig. 5(b) for reference.

Here, the sample temperature under laser irradiation was estimated using the abovementioned formula considering the thermal diffusion. The plotted line in Fig. 5(a) is in good agreement with the observed tendency in the power dependence of $|1/q|$ in the lower-power region. For bi- and tri-layers, the trends are similar not only in the low-power region but also in all measured power regions. Therefore, we conclude that the change in the relaxation time of electronic excited states in graphene due to the increased temperature may change the value of q as observed in the experiments.

- Higher-power region

By contrast, the observed increase of $|1/q|$ above 10 mW for 1 ML graphene [Fig. 4(a)] could not be explained by the abovementioned model. To explain this discrepancy, we consider the Fermi level shift owing to laser heating. Fermi energy should typically shift to the Dirac point when temperature goes up because of nonparabolicity of the band structure near the Fermi level [42], which can result in the change of the electron–phonon coupling V

in Eq. 1). Along this line, we calculated the laser-power dependence of the Fermi energy by assuming the density of state (DOS) of graphene as a linear function of E [43]. We used the following equation: $N = \int_0^\infty D(E)f(E_F, T, E)dE$ to estimate the Fermi level shift, where N is the electron density, $D(E)$ is DOS, $f(E_F, T, E)$ is the Fermi–Dirac function for a given Fermi energy E_F and temperature T. The initial Fermi energy $|E_F|$ is estimated by the resistivity measurement of the gated graphene device fabricated using the same procedure as the sample used in this experiment [44]. We calculate the temperature-induced change in E_F so that the electron density N is kept constant. Then, we obtain the laser-power dependence of E_F using the abovementioned relation of power P and temperature change ΔT.

Using the Fermi energy dependence of the Fano asymmetry parameter obtained by Yoon et al. [21,25], we can estimate $|1/q|$ using E_F estimated by the temperature increase ΔT. Figure 5(c) indicates that the calculated dependence of $|1/q|$ on laser power (dashed red line) [i.e., ΔT] is in good agreement with that observed in the higher-power region when the initial Fermi level is 0.2 eV. An increase in $|1/q|$ occurs because when the temperature increases, the Fermi energy becomes smaller than the phonon energy of graphene, thus increasing the interaction between electrons and phonons and, consequently, increasing $|1/q|$. The estimated decrease of the Fermi level was 0.025 eV for the input power of 20 mW (the temperature of 700 K).

If we follow this interpretation, it is necessary to clarify why graphene or graphene with two or more layer numbers exhibits only a monotonical decrease in $|1/q|$ with laser power. There may be two reasons for this phenomenon. The first potential reason is enhancement of electron scattering owing to the splitting of electronic bands for multilayers [5,8,34]. This

leads to the faster relaxation of electronic excited states because of accelerated dephasing owing to scattering, which decreases phase difference between phononic and electronic responses; thus, the parameter $|1/q|$ is smaller, as illustrated in Eq. 2). The other possible reason is that the higher the layer number is, the smaller the change in the Fermi level with temperature owing to the change in the band structure and DOS. For any stacking order of the layers, DOS near the Dirac point increases, which lowers the asymmetry of DOS and the Fermi level shift. These alterations may result in a smaller change of 1/q with a change in the laser power observed in this experiment. Further elaborated research should be required to prove the validity of the model.

Conclusion

In conclusion, we visualized the phase difference of electron–electron coupling and electron–phonon coupling from the Fano asymmetry parameter q of G-band phonons in a multilayer graphene stack. The asymmetry parameter q was obtained by fitting the G-band spectra to the BWF function convoluted with the Gauss function. The value of $|1/q|$ decreases with the layer number and excitation power in the low-power region for monolayer graphene, which is interpreted in terms of the temperature-induced phase shift between the discrete phonon state and the electron continuum. Similar trends were observed for bilayer, trilayer, and thicker-layer graphene. In contrast to this trend, in the higher-power region for monolayer graphene, $|1/q|$ increases with laser power. This behavior of $|1/q|$ for high-power excitation may be understood by laser-heating-induced Fermi energy shifts. The observed results of Fano interference images of the multilayer graphene stack provide a new perspective for the

future applications investigating the electron–phonon coupling and electron–electron coupling and temperature dependence.

Data Availability Statement

The data that support the findings of this study are available from the corresponding author upon reasonable request.

References

1. A. K. Geim, and K. S. Novoselov: Nat. Mater. **6**, 183 (2007).

2. A. K. Geim, K. S. Novoselov, S.V. Morozov, D. Jiang, S. V. Dubonos, I. V. Grigorieva, and A. A. Firsov: Science **306**, 666 (2004).

3. K. S. Novoselov, Z. Jiang, Y. Zhang, S. V. Morozov, H. L. Stormer, U. Zeitler, J. C. Maan, G. S. Boebinger, P. Kim, and A. K. Geim: Science **315**, 1379 (2007).

4. J. C. Meyer, A. K. Geim, M. I. Katsnelson, K. S. Novoselov, T. J. Booth, and S. Roth: Nature **446**, 60 (2007).

5. A. C. Ferrari, J. C. Meyer, V. Scardaci, C. Casiraghi, M. Lazzeri, F. Mauri, S. Piscanec,

D. Jiang, K. S. Novoselov, S. Roth, and A. K. Geim: Phys. Rev. Lett. **97**, 187401 (2006).

6. A. C. Ferrari: Sol. Stat. Commun. **143**, 47-57 (2007).

7. D. Graf, F. Molitor, K. Ensslin, C. Stampfer, A. Jungen, C. Hierold, and L. Wirtz: Nano Lett. **7**, 238-242 (2007).

8. D. Graf, F. Molitor, K. Ensslin, C. Stampfer, A. Jungen, C. Hierold, and L. Wirtz: Sol. Stat. Commun. **143**, 44-46 (2007).

9. A. Das, S. Pisana, B. Chakraborty, S. Piscanec, S. K. Saha, U. V. Waghmare, K. S. Novoselov, H. R. Krishnamurthy, A. K. Geim, A. C. Ferrari, and A. K. Sood: Nat. Nanotechnol. **3**, 210-215 (2008).

10. Z. Ni, Y. Wang, T. Yu Z. Shen: Nano Res. **1**, 273-291 (2008).

11. H. Wang, Y. Wang, X. Cao, M. Feng, G. Lan: J. Raman Spectrosc. **40**, 1791-1796 (2009).

12. R. W. Havener, H. Zhuang, L. Brown, R. G. Hennig, and J. Park: Nano Lett. **12**, 3162 (2012).

13. Y. Y. Wang, Z. H. Ni, and Z. X. Shen: Appl. Phys. Lett. **92**, 043121 (2008).

14. A. Eckmann, A. Felten, A. Mishchenko, L. Britnell, R. Krupke, K. S. Novoselov, and C. Cairaghi: Nano Lett. **12**, 3925-3930 (2012).

15. C. Stampfer, F. Molitor, D. Graf, and K. Ensslin: Appl. Phys. Lett. **91**, 241907 (2007).

16. J. Yan, Y. Zhang, P. Kim, and A. Pinczuk: Phys. Rev. Lett. **98**, 166802 (2007).

17. U. Fano: Phys. Rev. **124**, 1866-1878 (1961).

18. F. Cerdeira, T.A. Fjeldly, and M. Cardona: Phys. Rev. B **8**, 4734 (1973).

19. M.V. Klein, in *Light scattering in solids I, Topics in applied physics* (Springer-Verlag, Berlin, 1983) Vol. 8, pp. 147-204.

20. P. H. Tan, W. P. Han, W. J. Zhao, Z. H. Wu, K. Chang, H. Wang, Y. F. Wang, N. Bonini, N. Marzari, G. Savini, A. Lombardo, and A. C. Ferrari: Nature Mat. **11**, 294-300 (2014).

21. E. H. Hasedo, A. R. T. Nugraha, M. S. Dresselhaus and R. Saito: Phys. Rev. B **90**, 245140 (2014).

22. P. C. Eklund and K. R. Subbaswamy: Phys. Rev. B **20**, 5157 (1979).

23. S. D. M. Brown, A. Jorio, P. Corio, M. S. Dresselhaus, G. Dresselhaus, R. Saito, and K. Kneipp: Phys. Rev. B **63**, 155414 (2001).

24. C. Jiang, K. Kempa, J. Zhao, U. Schlecht, U. Kolb, T. Basche, M. Burghard, and A. Mews: Phys. Rev. B **66**, 161404 (2002).

25. D. Yoon, D. Jeong, H.-J. Lee, R. Saito, Y.-W. Son, H.-C. Li, and H. Cheong: Carbon **61**, 373 (2013).

26. A. B. Kuzmenko, L. Benfatto, E. Cappelluti, I Crassee, D. van der Marel, P. Blake, K. S. Novoselov, and A. K. Geim: Phys. Rev. Lett. **103**, 116804 (2009).

27. J. M. Baranowski, M. Mozdzonek, P. Dabrowski, K. Grodecki, P. Osewski, W. Kozlowski, M. Kopciuszynski, and W. Strupinski: Graphene **2**, 115-120 (2013).

28. R. Kitaura, Y. Miyata, R. Xiang, J. Hone, J. Kong, R. S. Ruoff, and S. Maruyama: J. Phys. Soc. Jpn. **84**, 121013 (2015).

29. X. Chen, P. Zhao, R. Xiang, S. Kim, J.-H. Cha, S. Chiashi, S. Maruyama: Carbon **94**, 810 (2015).

30. P. Zhao, S. Kim, X. Chen, E. Einarsson, M. Wang, Y. Song, H. Wang, S. Chiashi, R. Xiang, and S. Maruyama: ACS Nano **8**, 11631 (2014).

31. W. Zhang, J. Yan, C.-H. Chen, L. Lei, J.-L Kuo, Z. Shen, and L.-J. Li: Nat. Commun. **4**,

2074 (2013).

32. J.-B. Wu, M.-L. Lin, X. Cong, H.-N. Liu, and P.-H. Tan: Chem. Soc. Rev. **47**, 1822 (2018).

33. Y. Chen, and L. Dai: Appl. Opt. **55**, 4085 (2016).

34. L. M. Malard, J. Nilsson, D. C. Elias, J. C. Brant, F. Plentz, E. S. Alves, A. H. Castro Neto, and M. A. Pimenta: Phys. Rev. B **76**, 201401 (2007).

35. M. Hase, M. Kitajima, S. Nakashima, and K. Mizoguchi: Phys. Rev. Lett. **88**, 067401 (2002).

36. O.V. Misochko, K. Ishioka, M. Hase, and M. Kitajima: J. Phys.: Condens. Mater. **19**, 156227 (2007).

37. D. Huehn, A. Govolov, P. R. Gil, and W. J. Parak: Adv. Funct. Mater. **22**, 294 (2012).

38. M. Sparks: J. Appl. Phys. **47**, 837 (1976).

39. C. Ott, A. Kadum, P. Raith, K. Meyer, M. Laux, J. Evers, C. H. Keitel, C. H. Greene, and T. Pfeifer: Science **340**, 716 (2013).

40. K. Kato, Y. Hasegawa, K. Oguri, T. Tawara, T. Nishikawa, and H. Gotoh: Phys. Rev. B **97**, 104301 (2018).

41. S. Winnerl, M. Orlita, P. Plochocka, P. Kossacki, M. Potemski, T. Winzer, E. Malic, A. Knorr, M. Spinkle, C. Berger, W. A. de Heer, H. Schneider, and M. Helm: Phys. Rev. Lett. **107**, 237401 (2011).

42. N. W. Ashcroft and N. Mermin, *Solid State Physics* (Cengage Learning Inc., 1976) Chap. 2.

43. A. H. Castro Neto, F. Guinea, N. M. R. Peres, K. S. Novoselov, and A. K. Geim: Rev.

Mod. Phys. **81**, 109 (2009).

44. I. Katayama, K. Inoue, Y. Arashida, Y. Wu, H. Yang, T. Inoue, S. Chiashi, S. Maruyama, T. Nagao, M. Kitajima, and J. Takeda: Phys. Rev. B **101**, 245408 (2020).

Figure captions

Figure 1: Sample of the graphene stack and Raman maps. (a) Raman spectrum of monolayer graphene. The inset is an optical microscope image of the graphene multilayer stack. The area indicated by a red rectangle was examined by Raman mapping. (b) Raman intensity maps of the G peak, (c) Si optical phonon band, and (d) 2D peak. The hexagonal shape of graphene layers is also observed in Raman images. (e) Layer number dependence of the G-peak intensity. The G-band intensity is reported to increase almost linearly with layer number for sheets that are less than ~10 layers and then decrease for thicker graphene sheets [10,13]. The observed dependence is similar to the trend for thinner sheets.

Figure 2: Raman maps of (a) intensity I_G, (b) frequency f_G, (c) damping constant Γ_G, and (d) electron–phonon coupling strength $|1/q|$ for the G-band around the 1–2-ML border of the graphene stack. The data were obtained at a laser power of 0.23 mW. The values of f_G, Γ_G, and $|1/q|$ were obtained using BWF fittings at each scanning point. The maps clearly indicate the change in $|1/q|$, as well f_G and Γ_G, along the border.

Figure 3: Line shapes of the G peaks. (a) Raman spectra (filled circles), fits by the BWF formula (dashed lines), and fits by the BWF–Gauss function (solid lines). The data for 1- and 2-ML graphene and graphite are plotted. (b) Changes in line shapes owing to slight changes in $1/q$ values in the BWF–Gauss function. The plot ensures that $1/q$ values are clearly determined by the fitting. (c) Layer number dependence of the center frequency (f_G) and $1/q$ obtained by the BWF–Gauss fitting. The Raman spectra were obtained at a power of 0.23 mW. For the fitting, we used the spectra integrated over scanned positions on areas at each layer without defects. Error bars in the figure are estimated from the fitting accuracy of the parameter q.

Figure 4: Laser-power dependence of $1/q$ for 1, 2, and 3 ML of the graphene stack. The result for HOPG is also illustrated for comparison. The value of $1/q$ monotonously decreases with laser power, except for 1 ML. Dashed lines are guidelines for the experimental data points. The $|1/q|$ images for the 1–2-ML border measured at 10- and 20-mW laser powers are presented on the right-hand side. The circle indicates discrepancy from the monotonic decrease in $1/q$ for the 1-ML sample.

Figure 5: (a) Comparison of the observation and calculations for the laser-power dependence of $1/q$ for monolayer graphene. Circle: experiments; blue dotted line: extrapolation for temperature from the temperature dependence in reference [40]; red dashed line: calculated curve obtained by taking into account the laser-heating-induced Fermi energy change. (b) Relation of $1/q$ vs. the phase between discrete phonons and the

electronic continuum calculated using Eq. 2) [39]. In this figure, the observed values are plotted in green circles, together with the values of Si for comparison (blue triangles) [40]. (c) Laser-power dependence of calculated $1/q$ for monolayer graphene with different initial Fermi energies $|E_F^0|$ without laser excitation. Brown dotted line: $|E_F^0| = 0.10$ eV, pink dash-two-dot line: $|E_F^0| = 0.15$ eV, red solid line: $|E_F^0| = 0.20$ eV (this is the same as that of our sample), blue dash-dot line: $|E_F^0| = 0.25$ eV, green dotted line: $|E_F^0| = 0.30$ eV. We have also calculated the values for $|E_F^0| = 0$, which results in the same curve as that for $|E_F^0| = 0.15$ eV.
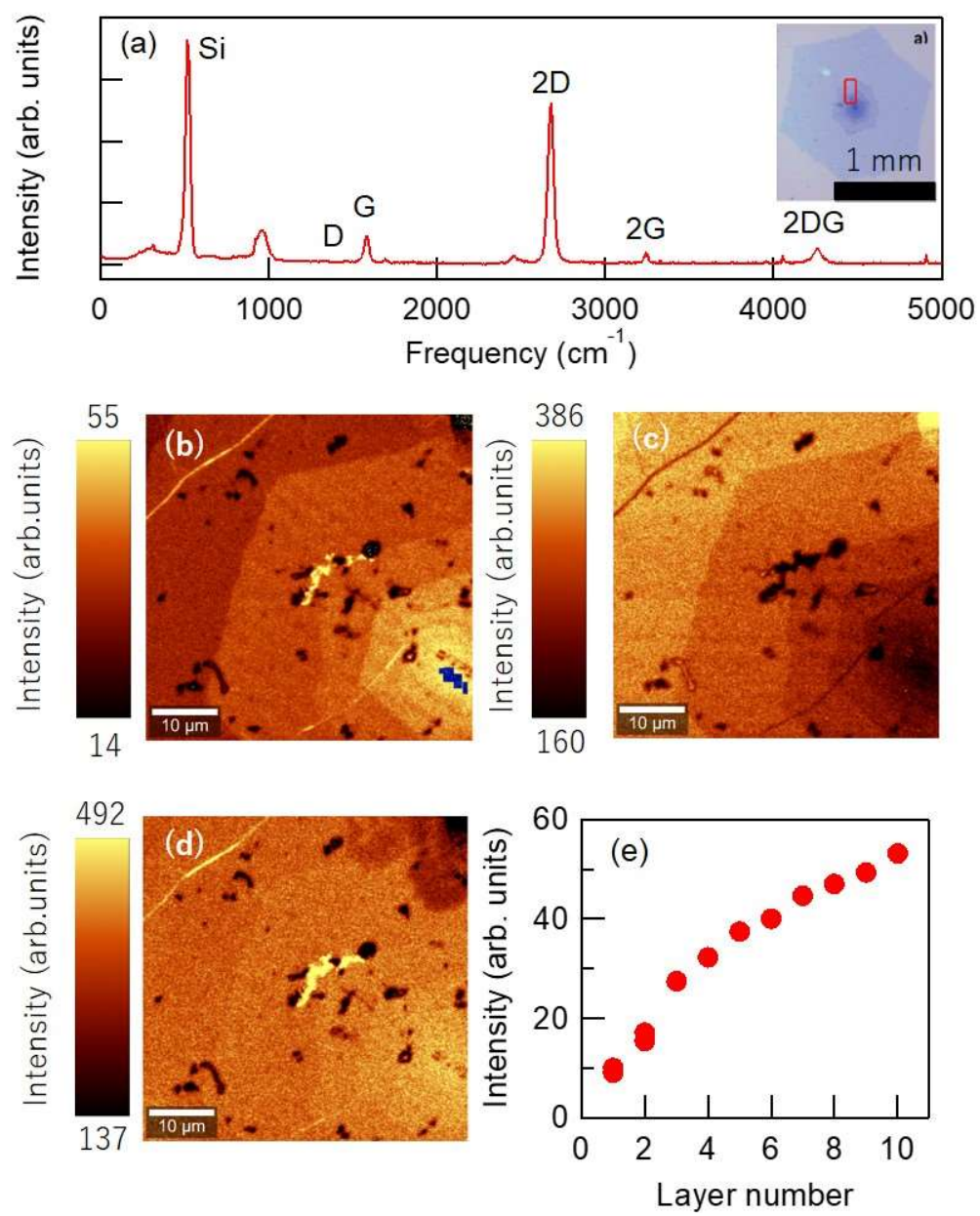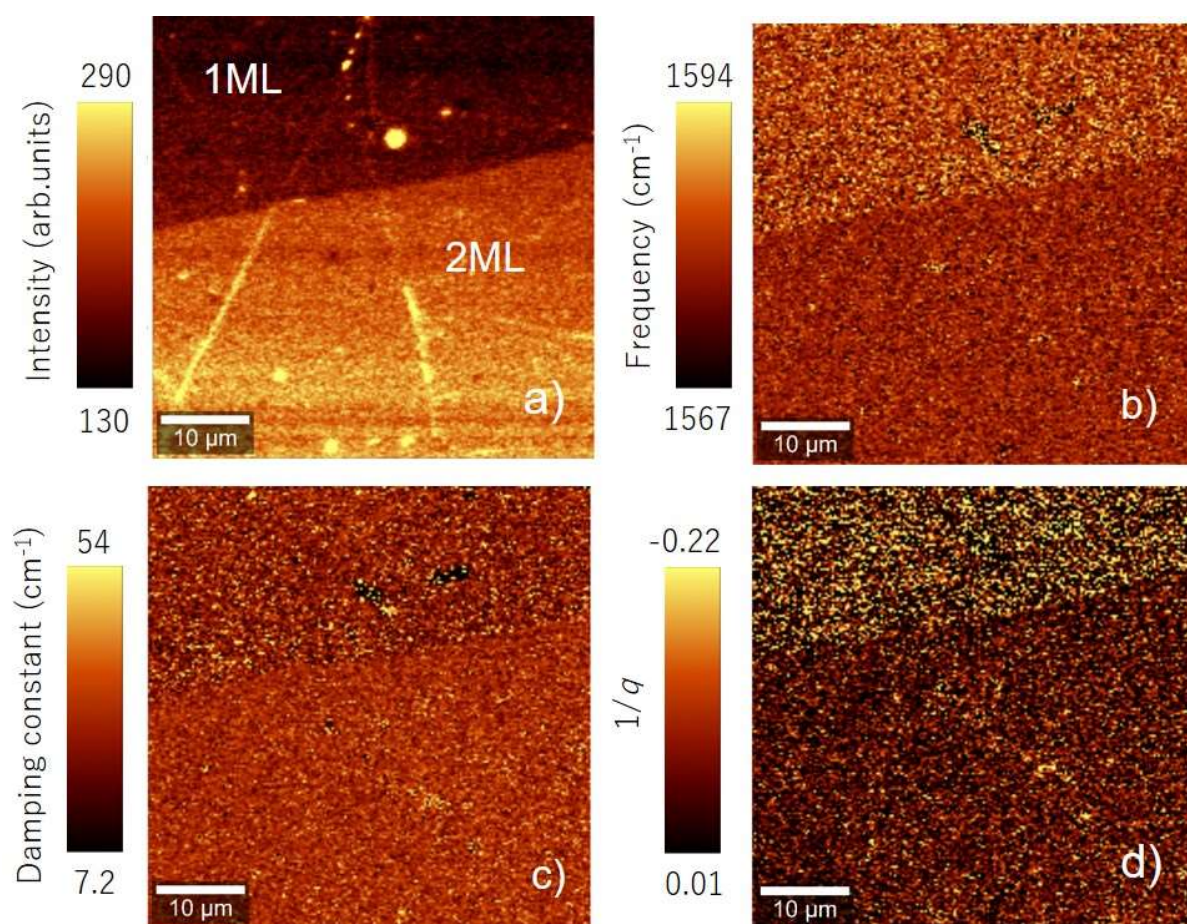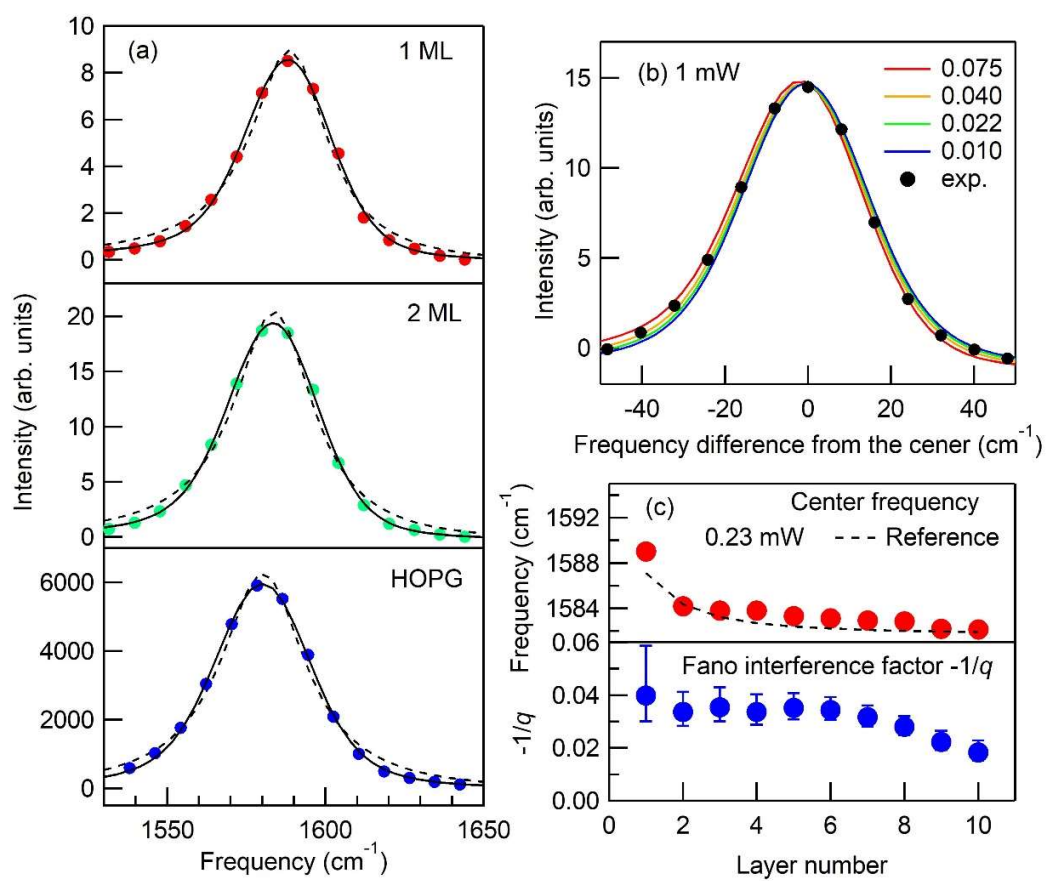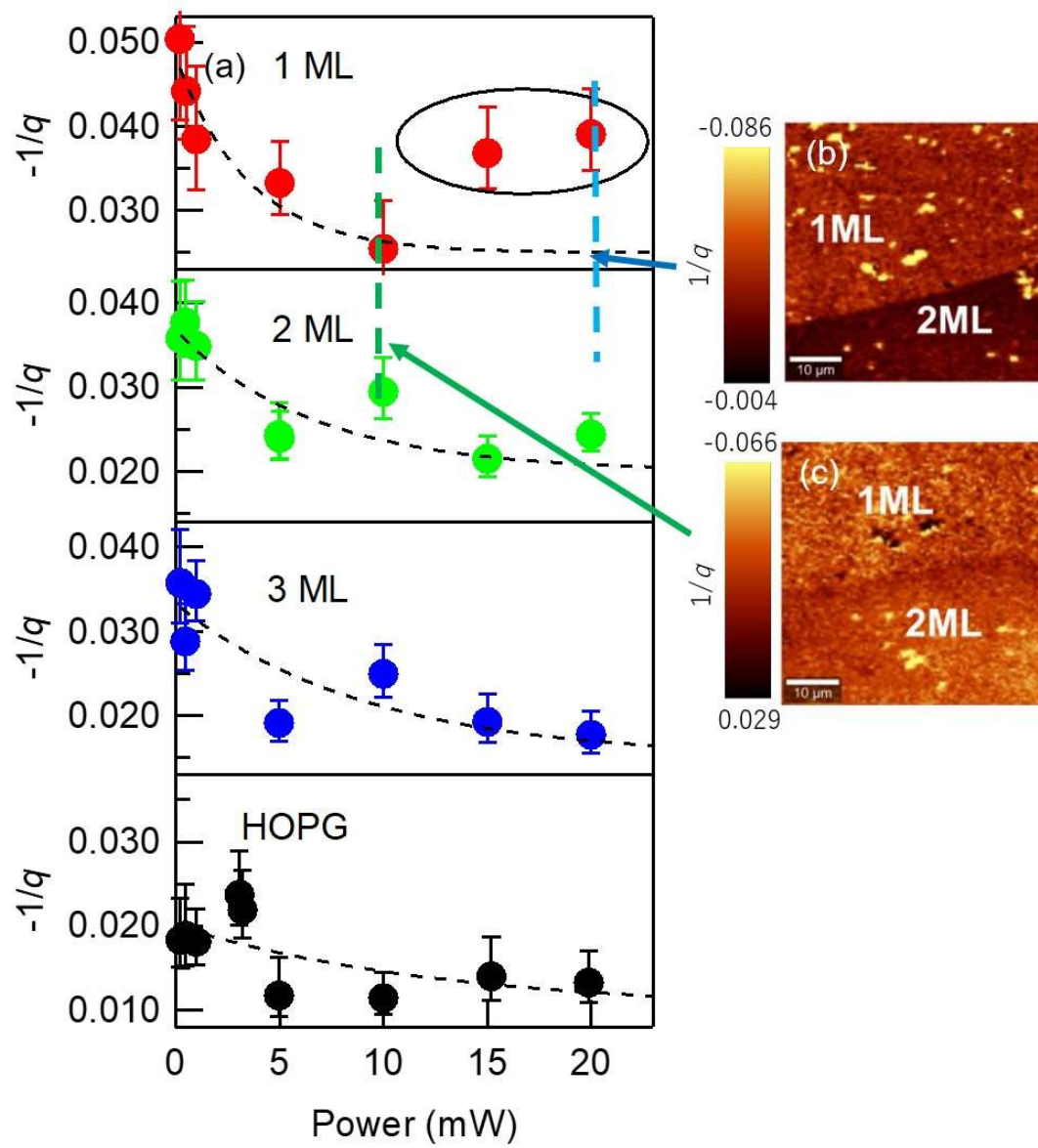
Fig. 1 Kitajima et al.

Fig. 2 Kitajima et al.

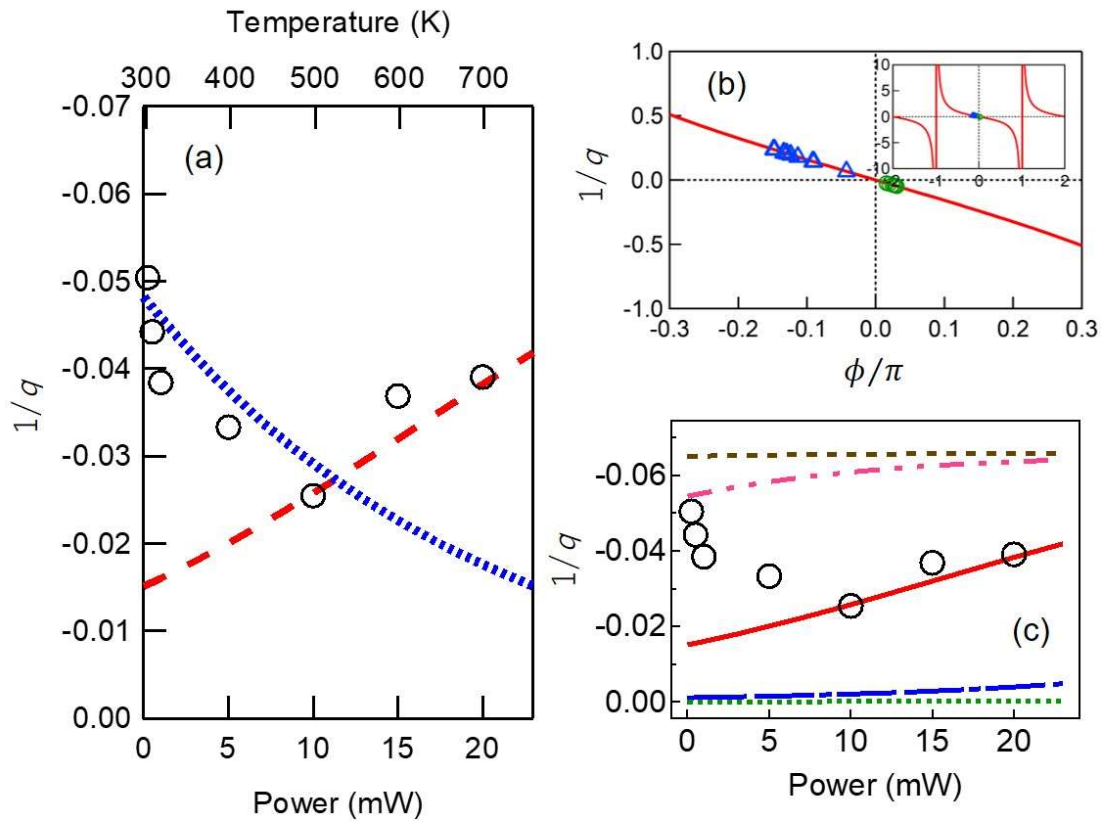Fig. 3 Kitajima et al.

Fig. 4 Kitajima et al.

Fig. 5 Kitajima et al.